Available online at www.sciencedirect.com
ScienceDirect
International Journal of Heat and Fluid Flow 28 (2007) 113–126
International Journal of HEAT AND FLUID FLOW
www.elsevier.com/locate/ijhff

Large eddy simulation of the generation and breakdown of a tumbling flow

Mauricio S. Toledo, Lionel Le Penven, Marc Buffat, Anne Cadiou *, Judith Padilla

Laboratoire de Mécanique des Fluides et d'Acoustique, UMR CNRS 5509, École Centrale de Lyon, 36 avenue Guy de Collongue, 69130 ECULLY, France
UFR de Mécanique, Université Claude Bernard Lyon 1, 48 boulevard du 11 Novembre 1918, 69622 Villeurbanne Cedex, France

Received 19 May 2005; received in revised form 2 March 2006; accepted 3 March 2006
Available online 27 June 2006

Abstract

Large eddy simulations (LES) are performed in order to reproduce the generation and the breakdown of a tumbling motion in the simplified model engine [Borée, J., Maurel, S., Bazile, R., 2002. Disruption of a compressed vortex. Phys. Fluids, 14 (7) 2543–2556]. A second-order accurate numerical scheme is applied in conjunction with a mixed finite volume/finite element formulation adapted for unstructured deforming meshes. Subgrid terms are kept as simple as possible with a Smagorinsky model in order to build a methodology devoted to engine-like flows. The main statistical quantities, such as mean velocity and turbulent kinetic energy, are obtained from a set of independent cycles and compared to experiments. Important experimental features, such as oscillations of the intake jet, vortex precession and a turbulent kinetic energy peak near the vortex core, are well reproduced.

Keywords: Engine flow; Tumble; LES; Unstructured mesh

1. Introduction

In the context of internal combustion engines, tumble is the name given to a large-scale vortical flow rotating about an axis perpendicular to the piston velocity (Lumley, 2001). Tumbling flows are generated during the intake phase by the inlet port, the cylinder head and the piston arrangement. Tumble flows are primarily employed to enhance the turbulence level during compression, just before ignition. High turbulence level increases the flame speed and the thermal efficiency, and makes the combustion more reliable under part load and lean burning conditions (Hill and Zhang, 1994). The production of turbulence is generally explained in terms of tumble breakdown occurring during compression. Conservation of angular momentum is expected to increase the tumble rotation rate during the compression stroke. Experimental works on motored engine configurations suggest that the tumble becomes instable at a compression ratio beyond 3 (Arcoumanis et al., 1990), leading to a strong decrease in the mean rotation rate and to production of turbulence.

The mechanisms involved in tumble generation and breakdown have been made more accessible by the experimental study of Marc et al. (1997) and Borée et al. (2002). In this experiment, a well organized and nearly two-dimensional tumble is observed at the end of intake. An intense peak of turbulence due to fluctuations correlated at a large-scale is located in this tumble core. During the compression stroke, an increase in the decay rate of the mean flow is observed beyond a volumetric ratio of order 2, associated to an energy transfer to turbulence. The mean flow structure evolution suggests that the vortex interaction with the walls plays an important role during compression.

Computational methods based on the Reynolds-averaged Navier–Stokes equations (RANS) are now essential to the process design of engine chambers. In the 1980s, RANS approaches were already used to study the influence of inlet arrangement and piston configuration on the

* Corresponding author. Tel.: +33 4 72 18 61 83; fax: +33 4 78 64 71 45.
E-mail address: anne.cadiou@ec-lyon.fr (A. Cadiou).

0142-727X/$ - see front matter © 2006 Elsevier Inc. All rights reserved.
doi:10.1016/j.ijheatfluidflow.2006.03.029

formation of the tumble (Gosman et al., 1985). In the experimental configuration of Marc et al. (1997), compared to standard K–ε model, Reynolds stress closures improve the prediction of the mean velocity because of their better capacity to take into account anisotropy and rotation effects (Le Roy and Le Penven, 1998). However, all models fail to predict the maximum of kinetic energy in the core of the tumble, observed experimentally.

In industrial context, RANS approach is extensively used because of its relatively low computational cost and its suitability to handle complex geometries. Thanks to the development of computers, large eddy simulation (LES) now becomes a promising tool. However, because of its higher computational cost in engine flow, contributions are quite recent (Celik et al., 2001; Haworth and Jansen, 2000; Moureau et al., 2004). Large eddy simulation (LES) approaches are aimed to predict the large-scale motions of turbulent flows from the low-pass filtered Navier–Stokes equations. The role of the smallest scales on the resolved ones is represented by subgrid-scale models. While conventional approaches based on RANS invoke a statistical description, LES results are particular realizations of the turbulent flow, corresponding to different initial and boundary conditions. For internal combustion engines, different flow realizations are equivalent to different engine cycles. LES approach is therefore expected to help the understanding of the cycle variability encountered in engine flows which has been much debated in the engine communauty (Lumley, 1999). LES also allows a more direct insight in the mechanisms responsible for the tumble breakdown that is still not well understood. In the recent years, much attention has been paid to the instabilities developing in flows having elliptic streamlines usually called elliptical instabilities (Kerswell, 2002). In tumble flows, the piston motion induces elliptical deformation of the streamlines during compression. This analogy suggests that elliptical-type instabilities play a role in the tumble collapse (Lumley, 2001; Le Roy and Le Penven, 1998). An investigation using proper orthogonal decomposition (POD) analysis on numerical and experimental dataset of engine flows has been recently performed by Fogleman et al. (2004). Numerical simulations of oblate (Lundgren and Mansour, 1996) and compressed (Le Ribault et al., in press) Taylor vortex show that turbulent transition can occur due to instability with respect to three-dimensional perturbation. However, in these studies, free slip boundary conditions are used and the effects of solid walls are not investigated.

In this paper, LES is applied to the tumbling flow studied by Borée et al. (2002). The developed numerical method retains choices that are also suitable for more complex engine flows. The experimental setup is described in Section 2. The filtered equations and the subgrid-scale model are detailed in Section 3. The numerical approach is explained in Section 4 where the simulation strategy is discussed. The influence of these choices is analysed in Section 5 and comparisons with the experimental data are also analysed.

2. The experimental database

The experimental set-up of Maurel (2001) consists in a squared cylinder equipped with a flat head piston of side $b = 100$ mm and moving sinusoidally at the angular velocity $\omega = 206$ rpm (see Fig. 1). The piston stroke is cyclic and consists in four successive phases, as in a real four-strokes engine. Defining the time $t = 0$ at the beginning of the intake stroke, the distance $a(t)$ from the piston to the cylinder head varies between $a_{\min} = 25$ mm and $a_{\max} = 100$ mm according to the sinusoidal law

$$a(t) = b - \frac{V_p}{\omega}(1 + \cos(\omega t)) \tag{1}$$

The compression ratio $r(t) = a_{\max}/a(t)$ reaches a maximum of 4. The maximum of the piston velocity is $V_p = 0.809$ m/s. The chamber is connected to a squared plenum of side 280 mm located upstream by an intake channel (300 mm length, $h = 10$ mm height and 96 mm width) through which the flow enters the chamber. The intake jet is deflected by the surface of the moving piston and creates a large-scale tumbling motion. At the end of the intake, the channel is closed by a guillotine device allowing the flow to be compressed. The channel remains closed during the expansion stroke and opens again for the exhaust. Then starts the intake phase of the next cycle, identical to the previous one. The order of magnitude of the velocity in the tumble can be taken as $V_p b/h$, which is the maximum value of the velocity in the intake channel. Based on this velocity scale, the chamber side length b and the viscosity at the end of the intake stroke, the Reynolds number defined by $Re = b^2 V_p/h\nu$ is equal to 54,000.

Throughout the paper, coordinates x, y and z will be taken as defined in Fig. 1, where x stands for the direction

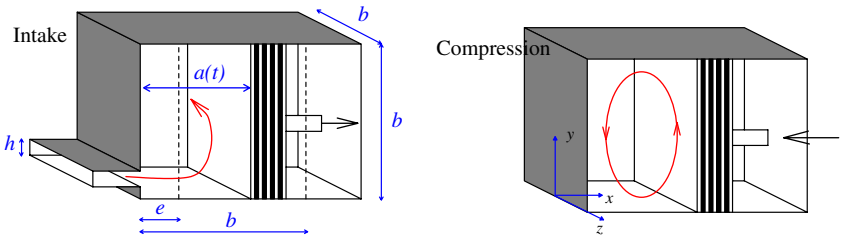

Fig. 1. Configurations during the intake and compression strokes.

of the piston motion. The plane $z = 0$ which delimits the flow domain in two symmetrical subvolumes will be referred to as the symmetry plane. The experimental database to which the simulations will be compared consists of 2D PIV velocity fields obtained in the symmetry plane and corresponding to different times of the intake and compression phases. The flow database analysed by Borée et al. (2002) consists of 120 cycles, giving access to mean and rms fields from the two components of the velocity in the plane $z = 0$. All physical quantities will be non-dimensionalized using the velocity V_p and the chamber height b.

3. Governing equations

The simulations described in the following are obtained using the formulation of the LES equations proposed by Vreman (1995). Denoting the effect of the spatial filter on a flow variable f by $\hat{f}$, the filtered equations for density, momentum and energy are written under the following form:

$$\frac{\partial \hat{\rho}}{\partial t} + \frac{\partial \hat{\rho}\tilde{u}_i}{\partial x_i} = 0 \tag{2}$$

$$\frac{\partial \hat{\rho}\tilde{u}_i}{\partial t} + \frac{\partial \hat{\rho}\tilde{u}_i\tilde{u}j}{\partial x_j} + \frac{\partial \hat{P}}{\partial x_i} - \frac{\partial \tilde{\sigma}_{ij}}{\partial x_j} = -\frac{\partial \tau_{ij}}{\partial x_j} + \frac{\partial(\hat{\sigma}_{ij} - \tilde{\sigma}_{ij})}{\partial x_j} \tag{3}$$

$$\frac{\partial \tilde{E}}{\partial t} + \frac{\partial(\tilde{E} + \hat{P})\tilde{u}_i}{\partial x_i} - \frac{\partial \tilde{\sigma}_{ij}\tilde{u}_j}{\partial x_i} + \frac{\partial \tilde{q}_i}{\partial x_i} = -a_1 - a_2 - a_3 + a_4 \tag{4}$$

This system is complemented by the filtered equation of state which reads, for perfect gases,

$$\hat{P} = \hat{\rho} R \tilde{T} \tag{5}$$

In Eqs. (2)–(4), the filtered density-weighted variables corresponding to velocity and temperature are denoted as $\tilde{u}_i$ and $\tilde{T}$. The variable $\tilde{E}$ is linked to the filtered pressure $\hat{P}$ by

$$\tilde{E} = \frac{\hat{P}}{\gamma - 1} + \frac{1}{2}\hat{\rho}\tilde{u}_i\tilde{u}_i \tag{6}$$

where γ is the ratio of the specific heats. The resolved heat flux vector $\tilde{q}_i$ and viscous stress tensor $\tilde{\sigma}_{ij}$ are defined by

$$\tilde{q}_i = -k(\tilde{T})\frac{\partial \tilde{T}}{\partial x_i} \tag{7}$$

$$\tilde{\sigma}_{ij} = \mu(\tilde{T})\left(\frac{\partial \tilde{u}_i}{\partial x_j} + \frac{\partial \tilde{u}_j}{\partial x_i} - \frac{2}{3}\frac{\partial \tilde{u}_k}{\partial x_k}\delta_{ij}\right) \tag{8}$$

where $k(\tilde{T})$ and $\mu(\tilde{T})$ are the thermal conductibility and the dynamic viscosity of the fluid.

In Eqs. (2)–(4), the left-hand side is expressed as functions of the resolved variables, $\hat{\rho}$, $\tilde{u}_i$, $\hat{P}$ and $\tilde{T}$. The right-hand side represents the effect of the unresolved eddies over the resolved ones and requires specific closures. Among all these terms, the subgrid stress tensor is defined as

$$\tau_{ij} = \hat{\rho}(\widetilde{u_i u_j} - \tilde{u}_i\tilde{u}_j) \tag{9}$$

Another contribution is due to the nonlinearity of the viscous term represented by $(\hat{\sigma}_{ij} - \tilde{\sigma}_{ij})$, where $\hat{\sigma}_{ij}$ is the filtered viscous strain. The three unknown terms a_1, a_2 and a_3 in the energy equation (4) read as follows:

$$a_1 = \tilde{u}_i\frac{\partial \tau_{ij}}{\partial x_j}, \quad a_2 = \frac{1}{\gamma - 1}\frac{\partial(\widehat{Pu_j} - \hat{P}\tilde{u}_j)}{\partial x_j},$$

$$a_3 = P\widehat{\frac{\partial u_j}{\partial x_j}} - \hat{P}\frac{\partial \tilde{u}_j}{\partial x_j} \tag{10}$$

The term a_1 represents the kinetic energy transferred between the resolved eddies and the unresolved ones, a_2 and a_3 are subgrid terms corresponding to pressure–velocity and pressure–dilatation correlations. The term a_4, which is not explicited, includes the subgrid dissipation rate, the nonlinearity of the viscous and heat flux terms.

Variations of viscosity and conductibility with temperature are taken into account by means of the Sutherland's law

$$\mu(\tilde{T}) = \mu_0\left(\frac{\tilde{T}}{T_0}\right)^{\frac{3}{2}}\frac{\tilde{T} + 110.4}{T_0 + 110.4} \quad k(\tilde{T}) = \frac{\gamma}{\gamma - 1}\frac{R}{Pr}\mu(\tilde{T}) \tag{11}$$

with $T_0 = 273.16$ K, $\mu_0 = 1.711 \times 10^{-5}$ kg/(m s), $\gamma = 1.4$, $Pr = 0.72$ and $R = 287.1$ J/(kg K) for air.

3.1. Subgrid-scale modeling

The subgrid stress tensor is modeled using the Boussinesq assumption of subgrid viscosity

$$\tau_{ij} - \frac{1}{3}\tau_{kk}\delta_{ij} = -2\mu_{sgs}S^D_{ij} \quad \text{where } S^D_{ij} = \frac{1}{2}\left(\frac{\partial \tilde{u}_i}{\partial x_j} + \frac{\partial \tilde{u}_j}{\partial x_i} - \frac{2}{3}\frac{\partial \tilde{u}_k}{\partial x_k}\delta_{ij}\right) \tag{12}$$

The isotropic part of τ_{ij} is the subgrid kinetic energy. It is assumed to be negligible in comparison to the thermodynamic pressure. The pressure velocity correlation is related to a turbulent heat flux and is modeled using the Prandtl analogy

$$a_2 + a_3 = -\frac{\partial}{\partial x_j}\left(k_{sgs}\frac{\partial \tilde{T}}{\partial x_j}\right) = -\frac{\partial}{\partial x_j}\left(\mu_{sgs}\frac{R\gamma}{Pr(\gamma - 1)}\frac{\partial \tilde{T}}{\partial x_j}\right) \tag{13}$$

Finally, a_4 is neglected following the work of Vreman (1995).

The LES results presented hereafter are obtained using the standard Smagorinsky model

$$\mu_{sgs} = \hat{\rho}C_s^2\Delta^2\left(2S^D_{ij}S^D_{ij}\right)^{\frac{1}{2}} \tag{14}$$

where $\Delta = (V_{cell})^{1/3}$ is a length scale parameter related to the volume V_{cell} of the local cell in the computational grid.

Different values of the Smagorinsky constant C_s are reported in the literature. The classical value, $C_s = 0.18$, proposed by Schumann (1991) is based on the characteristics of the Kolmogorov inertial law. This choice is however far from being retained for practical applications as it often

overestimates the viscous dissipation. Several authors propose smaller values, as $C_s = 0.065$ for channel flows (Moin and Kim, 1982; Cabot, 1995). Erlebacher et al. (1992) suggest $C_s = 0.092$ for sheared compressible flows. McMillan and Ferziger (1979) take $C_s = 0.13$ after comparing a modeled subgrid stress tensor with the DNS counterpart. Deardoff (1970) chooses $C_s = 0.2$ for the decay of homogeneous isotropic turbulence and $C_s = 0.1$ for channel flows. Our choice follows this tendency and retains $C_s = 0.08$, even if there is no reason to believe that it is optimal. We will discuss more on this point in Section 5.3.

The expression of the subgrid viscosity (Eq. (14)) is generally corrected for wall vicinity effects. A damping function is applied in order to reduce the length scales near the wall. Following the work of van Driest (1956), the damping coefficient used in the present simulations is defined by

$$D(y^+) = 1 - e^{-\frac{y^+}{25}} \tag{15}$$

where y^+ is the ratio between the distance to the nearest wall and the viscous length scale based on the friction velocity. In addition, the walls are supposed to be thermally isolated and the no-slip condition is retained for the velocity.

4. Numerical approach

4.1. Spatial and time discretization

The numerical method used for the present simulations is based on a mixed finite volume/finite element discretization of the compressible Navier–Stokes equations (Duchamp de Lageneste, 1999). The mesh is obtained from a partition of the computational domain into tetrahedral elements. Finite volume cells are constructed around a given node by joining the centroid of each neighbouring tetrahedron with the middle of their common side. Diffusive and source terms are evaluated using a Galerkin method with a second-order finite element interpolation. Euler fluxes are computed by a finite volume formulation based on a Roe approximate Riemann solver with a second-order MUSCL interpolation of the cell interface variables. To avoid the excessive dissipation introduced by this kind of method, the numerical scheme is formulated with two adjustable coefficients, α and κ, respectively, linked to the dissipation and dispersion errors of the numerical scheme. For the standard Roe scheme, $\alpha = 0.5$ and $\kappa = 1.0$. According to Carpentier (1995) and Duchamp de Lageneste (1999), these parameters can be adjusted to $\alpha = 0.1$ and $\kappa = 1/3$ in order to minimize the dissipation error for subsonic flows. This modification makes the numerical diffusion about 15 times lower than the standard Roe scheme while preserving numerical stability. In addition, the preconditioning technique introduced by Turkel (1987) is applied to ensure reasonable performance at low Mach numbers. Time integration is carried out with an explicit fourth-order Runge–Kutta scheme. For practical implementation, the solver is parallelized using MPI library and the present simulations have been performed on a parallel computer using 128 processors.

To handle the deformation of the domain, the equations are discretized on a moving mesh obtained by a coordinate transformation. As grid topology is conserved in this transformation, no interpolation is needed to take into account the mesh deformation. The influence of this approach on the overall behaviour of the numerical method has been analysed using a test case consisting of a vortex convected in an otherwise uniform inviscid subsonic flow (Poinsot and Lele, 1992; Visbal and Gaitonde, 1999). The computational domain, defined in the above references and rectangular in the (x, y) plane, is discretized with four unstructured regular meshes of $20 \times 40 \times 3$, $30 \times 60 \times 3$, $40 \times 80 \times 3$ and $80 \times 160 \times 3$ points in the x, y and z directions and the vortex is described with 11, 15, 21 and 39 nodes, respectively. Periodic conditions are applied in the x (along which the vortex is convected) and the z (for 2D approximation) directions. A symmetry condition is applied in y direction. After one convective time, the vortex is compared to the initial one and the L^2 norm of the y-velocity profiles at $x = 0$ at the mid-plane of the box is calculated for every mesh. In order to evaluate the influence of the mesh distortion on the error, the regular meshes are perturbed by a random displacement of the inner points on a sphere with a maximum radius of 40% of the average edge cell length. As shown in Fig. 2, a second-order accuracy is found when the vortex is resolved with a reasonable error level. The influence of the mesh displacement is tested by a periodic contraction and expansion of the inner points in the y-direction (Moureau et al., 2005), in order to mimic the configuration encountered with the tumble flow. The contraction occurs six times during the vortex convection. The error in the vortex simulation is affected only marginally by this dynamic deformation as shown in Fig. 3 and the numerical scheme remains of second-order. Using the same code, LES simulations of a compressed Taylor vortex flow have been performed recently by Le Ribault et al. (in press) and validated against accurate results of a spectral code.

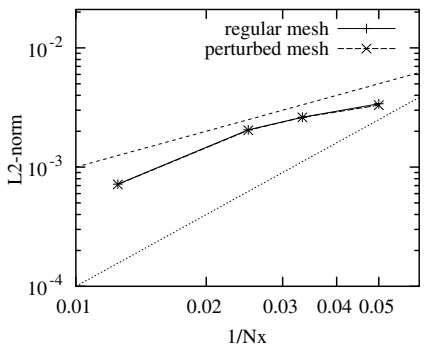

Fig. 2. Effect of grid resolution on the error for the vortex convection on a regular and a randomly perturbed mesh.

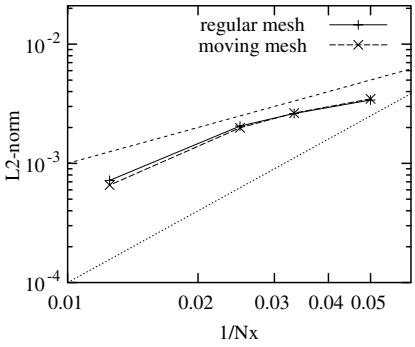

Fig. 3. Effect of grid resolution on the error for the vortex convection on a fixed and a moving mesh.

The numerical method has also been validated for various flow configurations as reported by Duchamp de Lageneste and Buffat (1998), Lakehal et al. (1998), Duchamp de Lageneste (1999), Le Ribault et al. (2002) and Buffat et al. (2004), and is implemented in a solver named as NadiaLES (http://www.codiciel.fr, 2004). The code has been developed at LMFA and is distributed under the CeCILL licence by the CNRS.

4.2. Computational domain

The geometry of the computational domain reproduces the compression chamber of Borée et al. (2002) (see Fig. 1). During the intake stroke, the computational domain is split into two parts: a fixed one corresponding to the intake channel ($x < 0$) and a deforming one for the chamber ($x > 0$). During the compression stroke, only the chamber is considered. A typical mesh used in the simulations has 10^6 tetrahedrons and it is refined near the solid walls to allow the application of the no-slip boundary condition.

4.3. Averaging

The present configuration, like practical engine flows, is statistically non-stationary in the sense that averaged properties are time-dependent. It is thus a situation where phase or ensemble averaging is required. In the present study, the statistical properties are estimated from averages on a finite number of cycles N. For any flow property $F(\theta, n)$ considered as a function of the phase-angle $\theta = \omega t$ and of the cycle index n, the phase averaged property $\overline{F}(\theta)$ is approached by

$$\overline{F}(\theta) = \frac{1}{N}\sum_{n=1}^{N} F(\theta, n) \tag{16}$$

Defining the fluctuation of the variable F by

$$f(\theta, n) = F(\theta, n) - \overline{F}(\theta) \tag{17}$$

the variance of the fluctuation is approached by

$$\overline{f^2}(\theta) = \frac{1}{N}\sum_{n=1}^{N} f^2(\theta, n) \tag{18}$$

This approximation is obviously so much better that N tends to infinity. Another way to obtain statistics is to apply time-average over moving intervals. In this procedure, the time interval must be larger than the turbulence time scale, but shorter than the time scale of the variations of the statistical properties of F. Much debate has emerged in the past in the engine research communauty on the benefits of each procedure. This question is not addressed in the present paper and just as Lumley (2001), we will consider turbulence as the deviation from the phase average.

4.4. Initial conditions and inflow boundary conditions

A straightforward strategy to simulate Internal Combustion engine flows consists in discretizing a large domain comprising the whole intake device (inlet manifold and an external plenum). The domain is often considered as closed, eliminating the need of inflow/outflow boundary conditions. This approach requires the computation of several four-stroke engine cycles to eliminate the influence of the initial conditions. This method is retained in the papers of Haworth and Jansen (2000) and Moureau et al. (2004). However, most of the studies only aim to predict the flow until ignition and the only reason to compute the power and exhaust strokes is to provide more realistic initial conditions for the next cycle.

An analogous problem can be found in more academic situations like turbulent channel flow. Perhaps the most straightforward approach would be to initiate the simulation far upstream the section of interest by a laminar profile excited with random perturbations in order to trigger turbulence. Again, this is a very expensive procedure and many attempts to define inflow conditions at short distances upstream the domain of interest can be found in the literature (Sagaut et al., 2004). By doing this, the CPU cost decreases because the computational domain is smaller and the delay for transition to turbulence is shortened.

A similar strategy can be retained for IC engine flows. Most of the studies only take into account intake and compression strokes. One can therefore easily figure that, if individual half-cycles can be computed, a more consistent database is obtained compared to four-stroke computations within the same CPU time. In the same way, the simplification of the computational domain can reduce the computational cost, allowing the use of a more refined grid where necessary. The major problem with the computation of individual cycles is the definition of initial and inflow conditions. In this section, a method is presented to specify these conditions at a reasonable cost in order to generalize LES to engine applications.

4.4.1. Initial conditions

The flow in the compression chamber, at the beginning of the intake stroke, is obtained by the method of Rogallo (1981). Basically, an incompressible, homogeneous, isotropic turbulent flow is generated in the Fourier space using a

Von Karman energy spectrum. The flow is defined on a 3D rectangular box with free-slip boundary conditions. It is then interpolated on the computational grid and the no-slip condition is applied from the first iteration. This initialization procedure has negligible impact on the CPU cost.

The parameters to be entered in the Rogallo procedure are the flow integral length scale and the kinetic energy. The integral length scale is expected to be a fraction of the clearance height. This parameter is set to 1/5 of this distance, in agreement with the size of the eddies observed in the experimental database at the end of exhaust. In the same way, the kinetic energy level corresponds to the volume-averaged value estimated from the experiment. The effect of initial kinetic energy level and integral length scale is analysed in Section 5.3.

4.4.2. Inflow boundary conditions

In the inlet section parallel to (y, z) plane, the velocity profile is supposed to be uniform except in thin boundary layers allowing the no-slip boundary conditions to be satisfied. The volume flow rate through the section is imposed to be equal to the volume swept by the piston per unit time. This assumption leads to velocity profiles in the intake channel in good agreement with the data of Maurel (2001). Random perturbations are imposed to the inlet flow by random forces during the whole intake stroke.

The random forces $\vec{f}(y, z, t)$ are defined on the inlet plane by a two-dimensional vector $\vec{f} = [0, f_y(y,z,t), f_z(y,z,t)]$ satisfying $\nabla \cdot \vec{f} = 0$ and $\vec{f} \cdot \vec{n}|_{\text{wall}} = 0$, where $\vec{n}$ denotes a unit vector normal to the side walls. The forces are time and space correlated functions generated by the generalized Langevin equation

$$\frac{\partial \vec{f}(y,z,t)}{\partial t} = -\frac{1}{t_c}\vec{f}(y,z,t) + \sigma \vec{W}(y,z,t) \tag{19}$$

The random function $\vec{W}$ is a zero-mean Gaussian white noise in time. At every time, $\vec{W}$ is generated in the Fourier space by the method of Rogallo (1981). This procedure amounts to imposing some spatial correlation property to the force $\vec{f}$. The one-point autocorrelation of $\vec{f}$ behaves for large time as

$$\overline{\vec{f}(y,z,t)\vec{f}(y,z,t+\Delta t)} \sim \sigma^2 \, \mathrm{e}^{-\frac{|\Delta t|}{t_c}} \tag{20}$$

showing that t_c approaches the integral time scale. This parameter has to be specified along with the intensity σ and the space correlation scale of $\vec{W}$. The latter has been fixed to one-third of the channel height and the procedure has been tested with respect to the other two parameters. The time-scale parameter has a visible effect as shown by the isosurfaces of the vorticity magnitude plotted in Figs. 4 and 5. If the time scale is smaller than the time a vortex takes to travel from the entrance of the intake channel to the compression chamber, then the flow at the exit of the channel is not correlated with the inflow boundary condition. In the other case, the flow at the exit of the channel is strongly influenced by the inflow boundary condition.

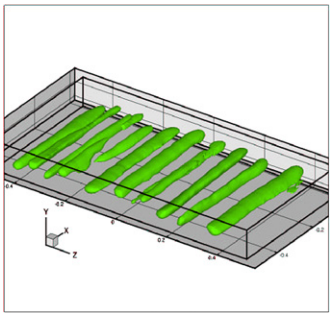

Fig. 4. $\sigma = 1.0$, $t_c = 0.5$.

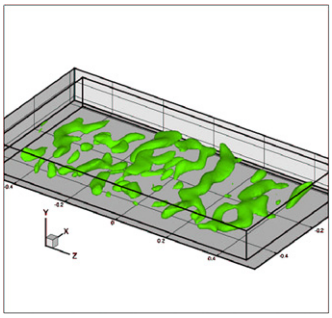

Fig. 5. $\sigma = 1.0$, $t_c = 0.03$.

The intensity of the force has a direct effect on the level of the velocity fluctuation in the intake channel. It must be large enough to introduce significative perturbation in the flow, but small enough to avoid the generation of excessive velocity gradients with respect to the rather coarse computational mesh used in the channel. For the present study, the couple of values $t_c = 0.03$ and $\sigma = 1.0$ generates an intensity of velocity fluctuations in the chamber similar to the one obtained by the random initialization procedure. Different tests have shown that the statistical properties of the flow developing in the chamber are only weakly sensitive to the values retained for these two parameters. In terms of CPU cost, this procedure increases up to 30% the time of one iteration. Both methods of generation of random conditions do not modify significantly the level of kinetic energy in the chamber in comparison with the case where the flow remains unperturbed.

5. Results

The numerical method described in the previous section has been applied to generate 10 independent realizations corresponding to the intake and compression phases of the experiment of Borée et al. (2002). The objective of this section is to compare the statistical properties of these numerical results to the experimental data. Additional information is also given to present certain properties of the procedure. We first consider a particular realization in order to describe qualitatively the flow evolution and identify the main features reported in the experimental work. One major characteristic is the high sensitivity of

the LES to initial disturbances and, hence, its capacity to generate turbulence. This will be attested by observation of velocity profiles and kinetic energy evolution. One interesting aspect of LES is to also give information about the three-dimensional behaviour of the flow, which is not provided in the experimental database. The simulation at $Re = 54{,}000$ will be compared to those obtained at lower values of the Reynolds number in order to highlight the properties which are specific to the flow in the experimental conditions.

In the following, V and W stand for the velocity components along y and z coordinates (vertical and normal directions, respectively) and U is the velocity along x (horizontal) direction from which the piston-induced velocity $x\dot{a}/a$ has been removed. The overline attribute $\overline{(\cdot)}$ will be used to represent ensemble (or phase) quantities. The fluctuations of U, V and W will be denoted as u, v and w. Spatial-averaged quantities obtained by integration over the chamber volume will be indicated by using the brackets symbols $\langle\cdot\rangle$. The three orthogonal planes passing through the center of the chamber and parallel to the coordinates planes will be referred to as the symmetry plane, the vertical and the horizontal plane (parallel to (x, y), (y, z) and (x, z), respectively). The velocity vectors are interpolated on regular and coarser grids to improve clarity of visualization. All profiles are plotted along the middle vertical and horizontal straight lines on the symmetry plane. All quantities are non-dimensionalized using the maximum piston velocity V_p and the chamber width b.

5.1. Characterization of the flow under experimental conditions

The LES corresponding to the Reynolds number value of the experiment are hereafter referred to as the high Reynolds number cases. Figs. 6 and 7 are relative to one particular realization of the flow and form a sequence of snapshots showing the normal component of vorticity on the symmetry plane. One can observe the boundary layers separating at the edges of the intake channel and the development of two counter-rotative vortices due to the roll-up of the upper and lower mixing layers of the jet. These vortices are strongly influenced by the piston, which deflects

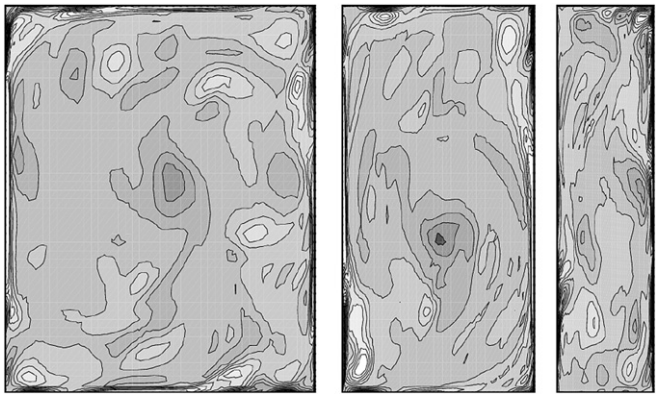

Fig. 7. z-Component of the dimensionless vorticity during the compression stroke.

both of them. The upper shear layer undergoes periodic eddy-detachment. This layer develops along the surface of the piston and generates a large-scale tumble with positive vorticity. By observing the tumble with a better time resolution, an anticlockwise precession of the vortex core can be seen around the center of the chamber. During the compression stroke, a complex distribution of vorticity emerges and the presence of the tumble is less easily identifiable. This is an indication of the disruption of the tumble, as reported by Borée et al. (2002).

Another interesting question is the three-dimensional character of the flow. Fig. 8 shows the projections of velocity field at the end of intake on the symmetry plane, the vertical and the horizontal plane. The velocity field corresponding to the end of compression is shown in Fig. 9. The views on the symmetry plane confirm the existence of a large-scale tumble at the end of intake and show a more complex organization of the flow at the end of compression. The views on the secondary planes indicate that the flow becomes progressively three-dimensional. At the end of compression, the symmetry is completely lost and the three components of the velocity field have similar importance. This isotropization of the flow is associated with the development of many vortices whose size is comparable to the clearance height. One important characteristic of the flow is that the details observed at the end of compression are very sensitive to the choice of the initial

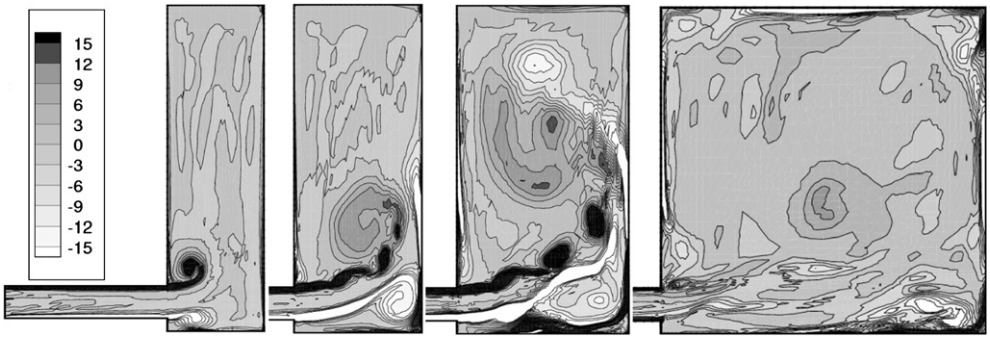

Fig. 6. z-Component of the dimensionless vorticity during the intake stroke.

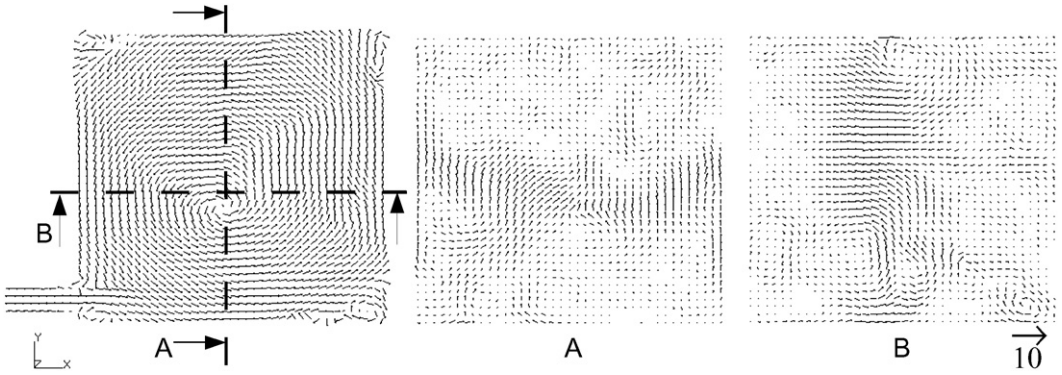

Fig. 8. Dimensionless velocity field on the symmetry plane, vertical plane A and horizontal plane B at the end of the intake stroke.

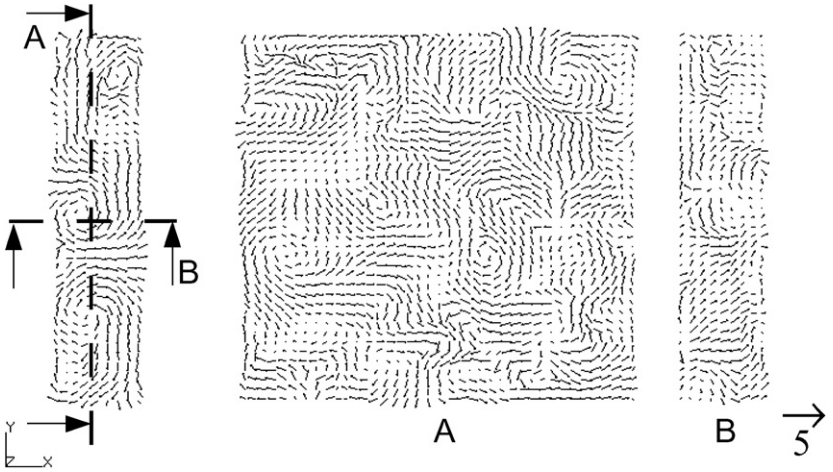

Fig. 9. Dimensionless velocity field on the symmetry plane, vertical plane A and horizontal plane B at the end of the compression stroke.

conditions. This fact is demonstrated in Figs. 10 and 11 where different velocity profiles corresponding to five independent realizations are shown. The variations displayed by the profiles at the end of intake can be explained by inspection of the continuous time sequences. These variations appear to be associated mostly to important fluctuations of the jet impact zone and to the variations of position of the vortex core. The former are due to rather small-scale eddies while the latter are associated to the large-scale precession motion. As shown in Fig. 11, the variations observed at the end of intake are strongly amplified, resulting in very different velocity profiles at the end of compression stroke. The sensitivity to initial conditions, the three-dimensionalization of the flow and the propensity to produce small scales are common characteristics of turbulent flows.

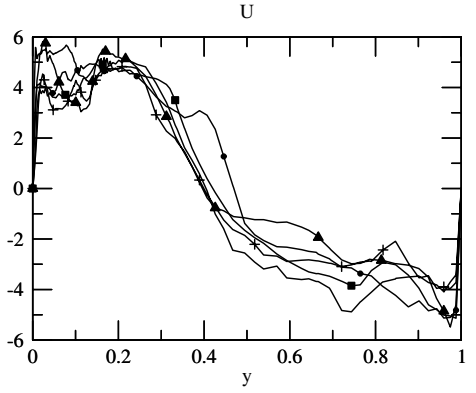

Fig. 10. Velocity profiles at the end of the intake stroke for different realizations.

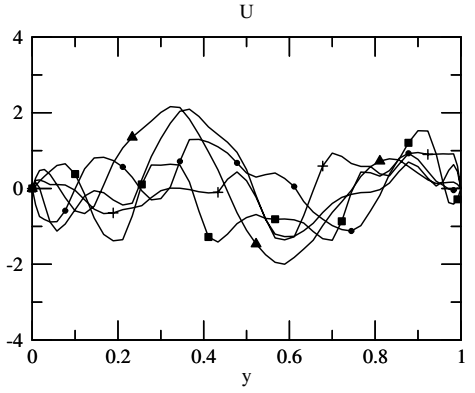

Fig. 11. Velocity profiles at the end of the compression stroke for different realizations.

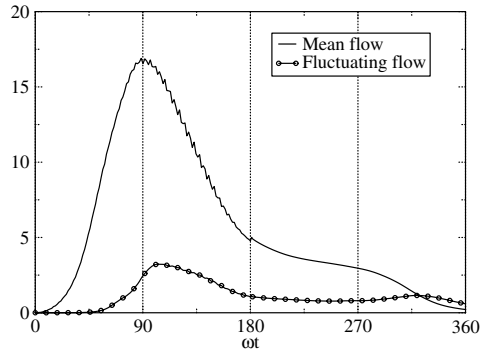

Fig. 12. Time evolution of the dimensionless volume averaged kinetic energy of the mean flow $\langle(\overline{U}^2+\overline{V}^2+\overline{W}^2)/2\rangle$ and the turbulent fluctuations $\langle(\overline{u^2}+\overline{v^2}+\overline{w^2})/2\rangle$.

Ten independent realizations have been simulated in order to compute the phase averaged statistics of the flow. Fig. 12 shows the time evolution of the volume-averaged kinetic energy associated to the mean flow $\langle(\overline{U}^2+\overline{V}^2+\overline{W}^2)/2\rangle$ and to the fluctuating flow $\langle(\overline{u^2}+\overline{v^2}+\overline{w^2})/2\rangle$, respectively. The kinetic energy of the mean flow grows as the flow enters the chamber. The maximum value is reached around $r=2$, when the piston velocity is maximum. In the second half of the intake stroke, when the piston decelerates, the kinetic energy decays and remains a decreasing function till the end of the compression phase. The kinetic energy of the fluctuating flow follows the same kind of variations during the intake stroke, with a certain delay, however, in the beginning of the growing phase. During the first half of the compression, the energy of the fluctuating field remains nearly constant, while the decay of the mean flow slows down. An increase of the fluctuating kinetic energy is observed in the last part of the compression stroke. The growing phase is associated to an acceleration of the decay of the mean flow. This final period corresponds to the extinction of the tumble, since most of the kinetic energy is contained in the fluctuating motion. Similar evolutions are reported in the experimental work of Borée et al. (2002). The contribution of each velocity component to kinetic energy is given in Table 1. At the end of intake, the kinetic energy of the mean flow is equally distributed to the x and y components, because the flow is dominated by the tumble which is nearly two-dimensional. On the other hand, the energy of the fluctuations is distributed quite isotropically and represents about 15% of the total kinetic energy. At the end of the compression stroke, the total kinetic energy is about 5 times lower, with a strong decrease of the velocities in the x-direction, parallel to the piston motion. The velocity fluctuations supply about 70% of the total kinetic energy, which is mostly generated by the components parallel to the piston.

Table 1
Contributions to the dimensionless kinetic energy from each velocity component ($C_s=0.08$, 10 realizations)

	$\langle\overline{U}^2\rangle$	$\langle\overline{V}^2\rangle$	$\langle\overline{W}^2\rangle$	$\langle\overline{u^2}\rangle$	$\langle\overline{v^2}\rangle$	$\langle\overline{w^2}\rangle$
End of intake stroke	4.77	4.60	0.20	0.83	0.69	0.60
End of compression stroke	0.11	0.22	0.09	0.23	0.51	0.44

5.2. Influence of the Reynolds number

The high sensitivity with respect to initial or inflow boundary conditions is the source of intense fluctuations, which are typical of the turbulence occurring at large Reynolds numbers. In order to point out the specific properties due to the large value of Re, different simulations have been carried out for three lower values of the Reynolds number: $Re=2500$, 1000 and 500. For each case, the flow evolving in the presence of random forces at inlet and initial perturbation (hereafter noted $\mathbf{u}'\neq 0$) is compared to the configuration where no perturbation is imposed ($\mathbf{u}'=0$). The importance of the perturbation is evaluated by $\Delta E_c/E_c$, where ΔE_c is the kinetic energy associated to the perturbation and averaged on volume of the chamber Ω defined by

$$\Delta E_c=\frac{1}{\Omega}\int\frac{1}{2}\left(\vec{\mathbf{U}}|_{\mathbf{u}'\neq 0}-\vec{\mathbf{U}}|_{\mathbf{u}'=0}\right)^2 d\Omega \tag{21}$$

and E_c is the averaged kinetic energy of the case with no perturbation

$$E_c=\frac{1}{\Omega}\int\frac{1}{2}\left(\vec{\mathbf{U}}^2|_{\mathbf{u}'=0}\right) d\Omega \tag{22}$$

The time evolutions of E_c and $\Delta E_c/E_c$ are plotted in Fig. 14. For every value of Re, E_c grows in the first half part of the intake stroke and decreases till the end of the compression. The level of E_c is an increasing function of Re. In the late compression, an acceleration of the energy decay is observed in the high Reynolds number case, as in the previous section, but not in the three lower Re flows. The relative value $\Delta E_c/E_c$ exhibits significative change when Re varies from 1000 to 2500. At higher values, the perturbation grows sharply during the most part of the intake phase, remains constant or mildly decreases during the first part of compression and grows again rapidly in the final phase. For $Re=1000$ and $Re=500$, the perturbation level remains significantly lower, and is moreover damped during compression.

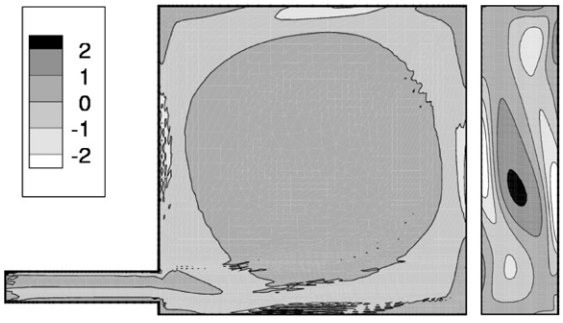

Fig. 13. z-Component of the dimensionless vorticity field at the end of the intake (left) and compression (right) stroke for $Re=1000$.

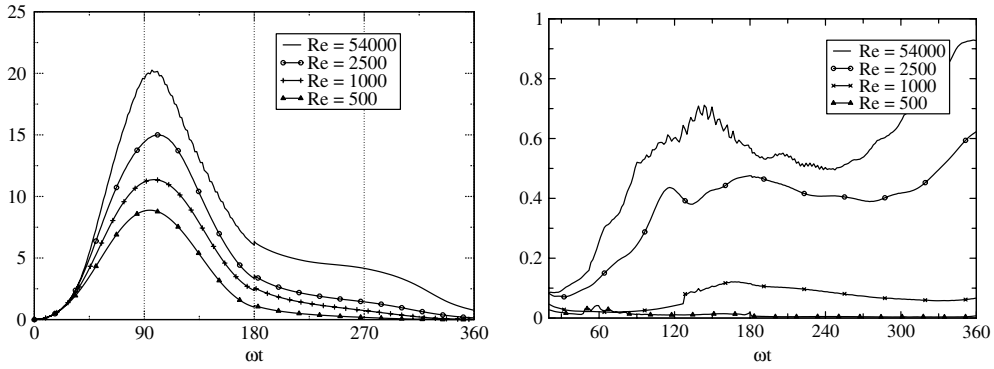

Fig. 14. Time evolution of the averaged kinetic energy E_c (left) and $\Delta E_c/E_c$ (right) during the intake and compression stroke.

Fig. 13 represents isolines of the normal component of the vorticity on the symmetry plane for the case $Re = 1000$. Compared to the high Reynolds case (Figs. 6 and 7), the flow structure appears to be more regular both at the end of intake and of compression. Movies of the time evolution show that the intake phase do not exhibit the flapping motion and the eddy detachment of the jet observed at the higher value of Re. The precession motion of the vortex center also appears to be very weak. At the end of intake, the different contributions to the kinetic energy are $\langle U^2\rangle = 2.38$, $\langle V^2\rangle = 2.27$ and $\langle W^2\rangle = 0.06$. The flow can be thus considered as two-dimensional. During the compression phase, the tumble remains discernible until the end of the compression stroke. Two secondary vortices arise when there are adverse pressure gradients at the upper right corner and the lower left corner of the chamber. At the end of the compression, the different contributions are $\langle U^2\rangle = 2.86\times10^{-2}$, $\langle V^2\rangle = 1.26\times10^{-1}$ and $\langle W^2\rangle = 1.88\times10^{-2}$. About 70% of the kinetic energy comes from $\langle V^2\rangle$. It is also important to note that for this low value of the Reynolds number, the symmetry of the flow with respect to the (x, y) plane is preserved till the end of the compression stroke.

5.3. Comments on initialization of LES and on subgrid modeling

As mentioned earlier, a certain amount of dispersion is observed in the values of the constant C_s of the Smagorinsky subgrid-scale model reported in the literature. While it seems feasible to associate a value of the parameter C_s to a defined class of academic flows, the optimal choice remains unknown for complex configurations. A set of five realizations has been obtained using the standard Smagorinsky coefficient $C_s = 0.18$, corresponding to the inlet and initial conditions of a subset of the database simulated with $C_s = 0.08$. Table 2 gives the corresponding distributions of the kinetic energy among the velocity components. At the end of the intake stroke, the statistics obtained with $C_s = 0.18$ give similar values for the contribution to kinetic energy of the mean flow, while the contributions to the kinetic energy of the fluctuations are 25% lower. At the end of compression, the latter are reduced by 10% and the mean flow appears to be more two-dimensional. Incidentally, by comparing to Table 1 obtained with 10 realizations, a comment can be made on the convergence of the statistics. At the end of intake, the influence of the number of realizations seems to be negligible. Since the compression amplifies the intensity of fluctuations, the statistics are expected to converge more slowly, as expressed by the differences obtained at the end of compression.

The method of generating independent realizations used the combined effect of random inlet flow and random initial conditions. All tests performed show that the results in terms of statistics are qualitatively the same whatever the origin of the perturbation. For instance, when the random forces are not applied to the inlet profile, the contributions to turbulent kinetic energy obtained from five realizations are $\langle\overline{u^2}\rangle = 0.71$, $\langle\overline{v^2}\rangle = 0.58$ and $\langle\overline{w^2}\rangle = 0.52$ at end of intake. These values compare well with the ones obtained in our LES database.

5.4. Comparison with experimental results

The ensemble-averaged results corresponding to the 10 simulated cycles are now compared with the experiment.

Table 2
Contributions to the dimensionless kinetic energy from each velocity component (five realizations)

	$\langle\overline{U}^2\rangle$	$\langle\overline{V}^2\rangle$	$\langle\overline{W}^2\rangle$	$\langle\overline{u^2}\rangle$	$\langle\overline{v^2}\rangle$	$\langle\overline{w^2}\rangle$
End of intake stroke ($C_s = 0.18$)	4.77	4.58	0.25	0.57	0.43	0.44
End of intake stroke ($C_s = 0.08$)	5.04	4.88	0.25	0.70	0.59	0.50
End of compression stroke ($C_s = 0.18$)	0.15	0.32	0.11	0.19	0.48	0.34
End of compression stroke ($C_s = 0.08$)	0.13	0.24	0.19	0.19	0.47	0.44

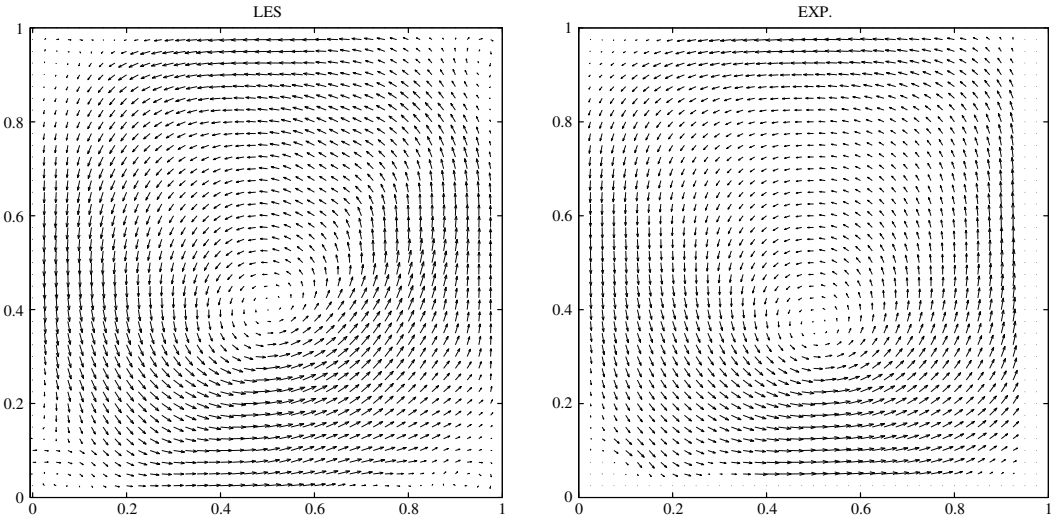

Fig. 15. Mean dimensionless velocity fields at the end of the intake stroke from simulation (left) and experiment (right).

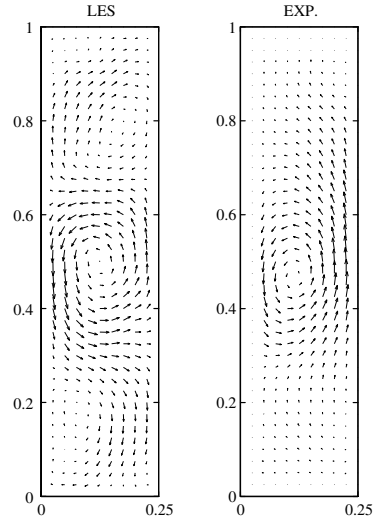

Fig. 16. Mean dimensionless velocity fields at the end of the compression stroke from simulation (left) and experiment (right).

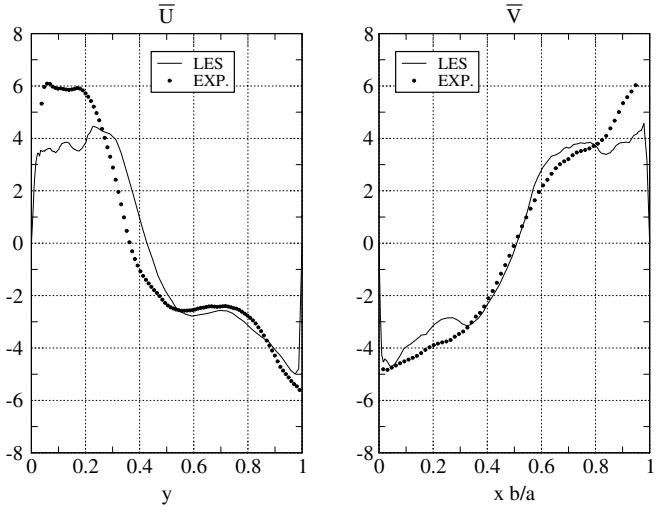

Fig. 17. Velocity profiles at the end of the intake stroke.

Mean velocity fields are shown in Figs. 15 and 16 at the end of intake and compression strokes. The tumble is correctly predicted at the end of intake, with a slight deviation of the vortex core. The mean flow weakens during compression due to viscosity effects and transfer of energy to the fluctuating flow. The last point is attested by the increasing variability between the different realizations. At the end of compression, the initial tumble becomes a nearly circular vortex in the middle of the chamber, observed in LES and experiment with comparable intensity. LES results show slight counter-rotative vortices in the upper and lower parts, which are not visible in the experiment. Mean velocity profiles are displayed in Fig. 17 at the end of intake. A good agreement is found despite the small number of cycles.

During compression, mean velocity profiles compare in much the same way. Figs. 18 and 19 correspond to the

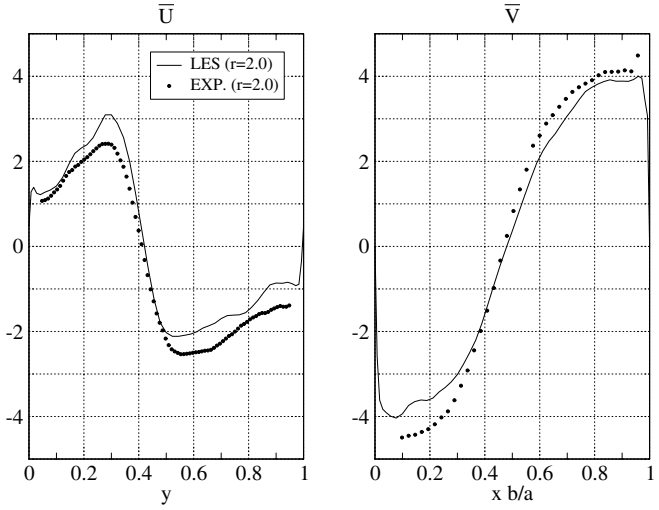

Fig. 18. Mean velocity profiles at $r = 2.0$.

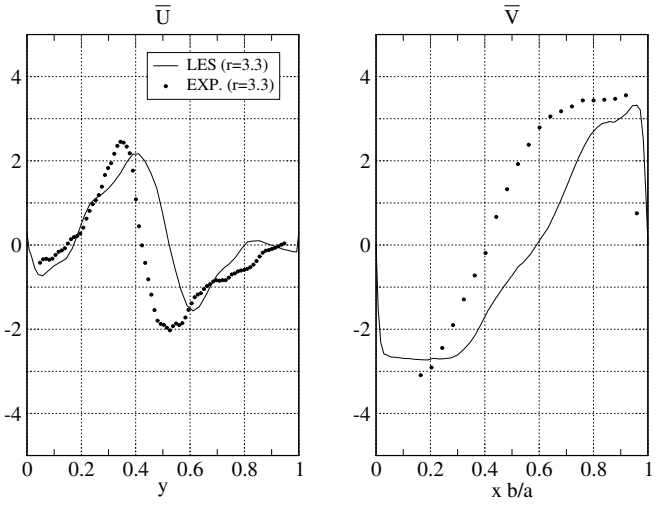

Fig. 19. Mean velocity profiles at $r = 3.3$.

compression ratio $r = 2.0$ and $r = 3.3$. A reasonable agreement is obtained on the velocity levels, however, differences increase somewhat in the late compression. In particular, the center of the tumble is slightly shifted at $r = 3.3$. Mean velocity profiles at the end of compression (Fig. 20) show two weak vortices on both sides of the tumble, as already noticed in Fig. 16.

The intensity of the fluctuating field is quantified by

$$e = \frac{1}{2}(\overline{u^2} + \overline{v^2}) \tag{23}$$

representing the contribution to the kinetic energy of the velocity components parallel to the (x, y) plane. The contribution of $\overline{w^2}$ is not taken into account because it is not provided by the experimental database. Fig. 21 shows the y profile of e at the end of intake on the line passing through the center. The most important feature, observed in experiment and LES, is an important maximum near the center. By using proper orthogonal decomposition (POD), Borée et al. (2002) have identified the peak in the velocity fluctuation as the consequence of large-scale velocity fluctuations due to the variations of position of the vortex center. The animated sequences obtained from the present LES show that these fluctuations are associated to the precession motion of the vortex center during intake. The experimental data indicate that the peak of kinetic energy around the tumble center persists during compression with a growing intensity. LES also predicts a peak of kinetic energy around the tumble center, as indicated in Fig. 22 ($r = 3.3$). The level of the peak of the kinetic energy is however lower than that in the experiment.

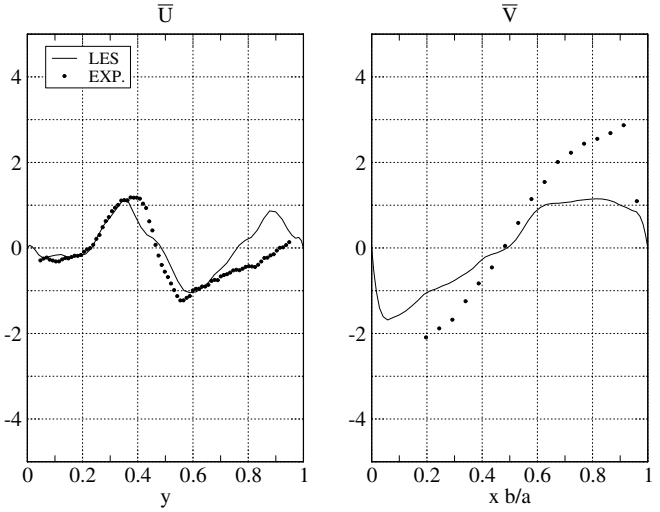

Fig. 20. Mean velocity profiles at end of compression.

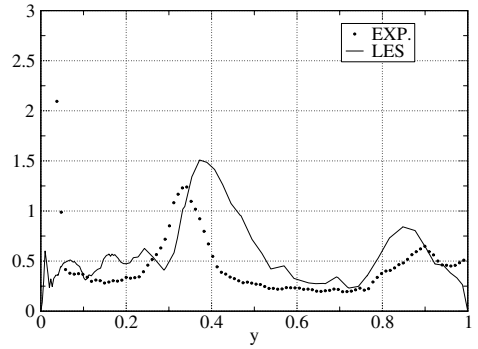

Fig. 21. Kinetic energy of the fluctuating flow. Vertical profile at the end of the intake stroke.

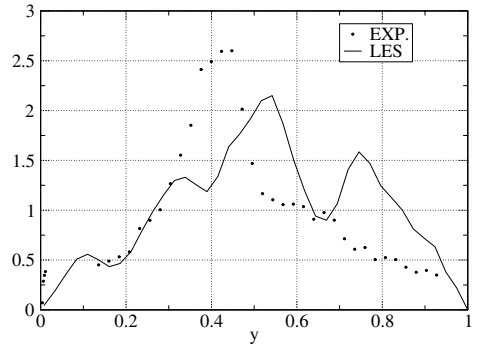

Fig. 22. Kinetic energy of the fluctuating flow. Vertical profiles at $r = 3.3$ during the compression.

As observed in the mean velocity and kinetic energy profiles, the overall agreement between experiment and simulation is satisfactory during intake, and gradually declines during compression. One possible reason is that the turbulence intensity grows during compression, thereby leading to a slower convergence of the statistics.

6. Concluding remarks

In the present study, large eddy simulations (LES) have been performed to reproduce the tumbling flow generated in the simplified model engine of Borée et al. (2002). The numerical approach is based on the resolution of the compressible Navier–Stokes equations using a mixed finite volume/finite element formulation on unstructured grids.

An upwind modified Roe scheme extended to second-order by a MUSCL interpolation is used to evaluate the Euler fluxes. The solution is advanced in time by an explicit fourth-order Runge–Kutta scheme. All simulations were performed using the Smagorinsky subgrid-scale model with a near wall correction. A method based on the generation of random inlet boundary conditions and initial flow fields has also been developed to simulate independent realizations. All these choices were guided with the intention to show that a LES method with relatively simple options can provide reasonable results in engine-like applications.

One interesting aspect of the LES methods is that they provide the time history of individual flow realizations. In the present study, a quite well organized tumble is formed on intake for every simulation. Secondary phenomena are also observed such as the flapping motion and the vortex shedding of the intake jet, and the precession of the tumble. The flow remains nearly two-dimensional until the early stage of compression. During the compression stroke, the flow is more three-dimensional and exhibits a complex behaviour. During the last part of compression, the trajectory of the tumble center is more erratic, and very sensitive to initial conditions. Statistics performed over 10 cycles allows to quantify the part of kinetic energy contained in the mean and in the fluctuating part of the flow. At the end of compression, most of the energy is associated to turbulence. The final mean flow is characterized by a weak, nearly circular vortex confined in the middle of the chamber.

The experimental results have been compared to the predictions of the 10 cycles obtained by simulation. At the end of the intake stroke, a reasonable agreement is found for the mean flow. The kinetic energy of the velocity fluctuations also compares well with the experimental profiles. Simulations show a peak of kinetic energy near the center of the chamber corresponding to the variations of position of the vortex core observed in the experiment. For a flow configuration very similar to the present one, it has been shown by Le Roy and Le Penven (1998) that the RANS approach using classical models such as K–ε and $\overline{u_i u_j}$–ε predicts a minimum of turbulent kinetic energy in the tumble core instead of the maximum observed in LES and experiment. As already mentioned, this maximum is associated to precession and to large-scale correlated fluctuations. In the context of engine applications, this kind of motion, usually referred to as cycle-to-cycle variations, has been widely discussed (Haworth, 1999). It is interesting to point out the capacity of LES to predict this kind of effect, called precessing vortex core, that can be found for example in swirling jets (Selle et al., 2004).

The peak of kinetic energy is shown to persist with a reasonable agreement during most of the compression stroke. At the end, the comparison is less satisfactory, the kinetic energy level being lower than that in the experiment. However, it must be pointed out that the convergence of the statistics is slower than for the intake phase since the compression amplifies the level of turbulence, thereby making the different realizations less correlated.

It is important to note that the present simulations have been performed with a second-order accurate numerical scheme, the most simple subgrid-scale model and a relatively coarse grid. It is interesting to keep the numerical method as simple as possible when dealing with engine-like applications and, from this point of view, the present results are quite encouraging. Despite the small number of cycles, a good qualitative agreement with experimental results is obtained.

Acknowledgments

This work was initially developed as a part of ARC Moteurs Propres et Economes supported by the CNRS, PSA and Renault. The authors would like to thank J. Borée for providing us with his PIV data. Maurício Silveira Toledo has benefited from a grant of the Brazilian CAPES Foundation. Simulations were carried out at the CINES.

References

Arcoumanis, C., Hu, Z., Vafidis, C., Whitelaw, J.H., 1990. Tumbling motion: a mechanism for turbulence enhancement in spark-ignition engines. SAE Paper 900060.

Borée, J., Maurel, S., Bazile, R., 2002. Disruption of a compressed vortex. Phys. Fluids 14 (7), 2543–2556.

Buffat, M., Cadiou, A., Le Penven, L., Le Ribault, C., 2004. Comparison of various implicit, explicit, centered and upwind schemes for the simulation of compressed flows on moving mesh. In: Mathematical and Numerical Aspects of Low Mach Number Flows, Porquerolles, France.

Cabot, W., 1995. Large-eddy simulation with wall models. Technical Report, CTR Annual Research Briefs.

Carpentier, R., 1995. Approximation et Analyse Numérique d'Ecoulements Instationnaires. PhD Thesis, Université de Nice Sofia-Antipolis.

Celik, I., Yavuz, I., Smirnov, A., 2001. Large-eddy simulations of in-cylinder turbulence for internal combustion engines: a review. Int. J. Engine Res. 2 (2), 119–148.

Deardoff, J.W., 1970. A numerical study of three-dimensional turbulent channel flow at large Reynolds numbers. J. Fluid Mech. 41, 453–465.

Duchamp de Lageneste, L., 1999. Simulation des Grandes Echelles d'Ecoulements Compressibles et Réactifs sur Maillages Non-Structurés. PhD Thesis, École Centrale de Lyon.

Duchamp de Lageneste, L., Buffat, M., 1998. Large eddy simulation of turbulent reactive flows on unstructured meshes. In: 16th International Conference on Numerical Methods in Fluid Dynamics, Arcachon, France.

Erlebacher, G., Hussaini, M.Y., Speziale, C.G., Zang, T.A., 1992. Towards the large-eddy simulation of compressible turbulent flows. J. Fluid Mech. 238, 155–185.

Fogleman, M., Lumley, J.L., Rempfer, D., Haworth, D., 2004. Application of the proper orthogonal decomposition to datasets of internal combustion engine flows. J. Turbul., 5/023:n.d. URL: http://jot.iop.org/.

Gosman, A.D., Tsui, Y.Y., Vafidis, C., 1985. Flow in a model engine with a shrouded valve—a combined experimental and computational study. SAE Paper 850498.

Haworth, D.C., 1999. Large-eddy simulation of in-cylinder flows. Oil Gas Sci. Technol. 54, 175–185.

Haworth, D.C., Jansen, K., 2000. Large-eddy simulation on unstructured deforming meshes: towards reciprocating IC engines. Comput. Fluids 29, 493–524.

Hill, P.G., Zhang, D., 1994. The effects of swirl and tumble on combustion in spark-ignition engines. Prog. Energy Combust. Sci. 20, 373.

Kerswell, R.R., 2002. Elliptical instability. Annu. Rev. Fluid Mech. 34, 83–113.

Lakehal, D., Duchamp de Lageneste, L., Thiele, F., Buffat, M., 1998. Computation of vortex-shedding flows past a square cylinder employing LES and RANS. In: Notes in Numerical Fluid Mechanics. Viewer Verlag.

Le Ribault, C., Le Penven, L., Buffat, M., 2002. LES and DNS of transition in the compressed Taylor vortex flow using a finite volume/finite element method. In: Third International Symposium on Finite Volume for Complex Applications, Porquerolles, 24–28 June.

Le Ribault, C. , Le Penven, L., Buffat, M., in press. LES of the compressed Taylor votex flow using a finite volume/finite element method on unstructured grids. Int. J. Numer. Method. Fluids.

Le Roy, O., Le Penven, L., 1998. Compression of a turbulent vortex flow. Int. J. Heat Fluid Flow 19, 533–540.

Lumley, J.L., 1999. Engines. An Introduction. Cambridge University Press, Cambridge.

Lumley, J.L., 2001. Early work on fluid mechanics in the IC engine. Annu. Rev. Fluid Mech. 33, 19–338.

Lundgren, T.S., Mansour, N.N., 1996. Transition to turbulence in an elliptic vortex. J. Fluid Mech. 307, 43–62.

Marc, D., Borée, J., Bazile, R., Charnay, G., 1997. Combined P.I.V. and L.D.V. analysis of the evolution and breakdown of a compressed tumbling vortex. In: 11th Symposium on Turbulent Shear Flows.

Maurel, S., 2001. Étude par imagerie laser de la génération et de la rupture d'un écoulement tourbillonnaire compressé. Situation modéle pour la validation de simulations aux grandes échelles dans les moteurs. PhD Thesis, Institut National Polytechnique de Toulouse.

McMillan, O.J., Ferziger, J.H., 1979. Direct testing of subgrid scale models. AIAA J. 17, 340–1346.

Moin, P., Kim, P., 1982. Numerical investigation of turbulent channel flow. J. Fluid Mech. 118, 341–377.

Moureau, V., Barton, I., Angelberger, C., Poinsot, T., 2004. Towards large eddy simulation in internal-combustion engines: simulation of a compressed tumble flow. SAE Paper 2004-01-1995.

Moureau, V., Lartigue, G., Sommerer, Y., Angelberger, C., Colin, O., Poinsot, T., 2005. Numerical methods for unsteady compressible multi-component reacting flows on fixed and moving grids. J. Comput. Phys. 202, 710–736.

Poinsot, T.J., Lele, S.K., 1992. Boundary conditions for direct simulations of compressible viscous flows. J. Comput. Phys. 101, 104–129.

Rogallo, R.S., 1981. Numerical experiments in homogeneous turbulence. Technical Report, NASA-TM-81315.

Sagaut, P., Gamier, E., Tromeur, E., Larchevêque, L., Labourasse, E., 2004. Turbulent inflow conditions for large-eddy simulation of compressible wall-bounded flows. AIAA J. 42 (3), 469–477.

Schumann, U., 1991. Direct and large-eddy simulation of turbulence—summary of the state-of-the-art. Technical Report, VKI Lecture Series 1991–02: Introduction to the Modeling of Turbulence.

Selle, L., Lartigue, G., Poinsot, T., Koch, R., Schildmacher, K.-U., Krebs, W., Prade, B., Kaufmann, P., Veynante, D., 2004. Compressible large eddy simulation of turbulent combustion in complex geometry on unstructured meshes. Combust. Flame 137, 489–505.

Turkel, E., 1987. Preconditioned methods for solving the incompressible and low speed compressible equations. J. Comput. Phys. 72, 277–298.

van Driest, E.R., 1956. On the turbulent flow near a wall. J. Aeronaut. Sci. 23, 1007–1011.

Visbal, M.R., Gaitonde, D.V., 1999. High-order-accurate methods for complex unsteady subsonic flows. AIAA J. 37 (10), 1231–1239.

Vreman, A.W., 1995. Direct and large-eddy simulation of the compressible turbulent mixing layer. PhD Thesis, University of Twente Enschede.